Commensurate versus incommensurate charge ordering near the superconducting dome in $Ir_{1-x}Pt_xTe_2$ revealed by resonant x-ray scattering

K. Takubo,[1,*] K. Yamamoto,[1] Y. Hirata,[1] H. Wadati,[1] T. Mizokawa,[2] R. Sutarto,[3] F. He,[3] K. Ishii,[4] Y. Yamasaki,[5] H. Nakao,[6]
Y. Murakami,[6] G. Matsuo,[7] H. Ishii,[7] M. Kobayashi,[7] K. Kudo,[7] and M. Nohara[7]

[1]*Institute for Solid State Physics, University of Tokyo, Kashiwa, Chiba 277-8581, Japan*
[2]*Department of Applied Physics, Waseda University, Okubo, Tokyo 169-8555, Japan*
[3]*Canadian Light Source, Saskatoon, Saskatchewan, Canada S7N 2V3*
[4]*Synchrotron Radiation Research Center, National Institutes for Quantum and Radiological Science and Technology, Hyogo 679-5148, Japan*
[5]*Research and Services Division of Materials Data and Integrated System (MaDIS), National Institute for Materials Science (NIMS),
Tsukuba 305-0047, Japan*
[6]*Institute of Materials Structure Science, High Energy Accelerator Research Organization, Tsukuba, Ibaraki 305-0801, Japan*
[7]*Research Institute for Interdisciplinary Science, Okayama University, Okayama 700-8530, Japan*

The electronic-structural modulations of $Ir_{1-x}Pt_xTe_2$ ($0 \leqq x \leqq 0.12$) have been examined by resonant elastic x-ray scattering (REXS) and resonant inelastic x-ray scattering (RIXS) techniques at both the Ir and Te edges. Charge-density-wave-like superstructures with wave vectors of $\mathbf{Q} = (1/5\ 0\ -1/5)$, $(1/8\ 0\ -1/8)$, and $(1/6\ 0\ -1/6)$ are observed on the same sample of IrTe₂ at the lowest temperature, the patterns of which are controlled by the cooling speeds. In contrast, superstructures around $\mathbf{Q} = (1/5\ 0\ -1/5)$ are observed for doped samples ($0.02 \leqq x \leqq 0.05$). The superstructure reflections persist to higher Pt substitution than previously assumed, demonstrating that a charge-density wave (CDW) can coexist with superconductivity. The analysis of the energy-dependent REXS and RIXS line shape reveals the importance of the Te $5p$ state rather than the Ir $5d$ states in the formation of the spatial modulation of these systems. The phase diagram reexamined in this work suggests that the CDW incommensurability may correlate with the emergence of superconducting states such as Cu_xTiSe_2 and Li_xTaS_2.

I. INTRODUCTION

The interplay between spin-orbit coupling and the Coulomb interaction led to a renaissance in the study of transition-metal compounds because it can lead to novel superconductivity competing with charge ordering of spin-orbit Mott states, as in high-T_C superconductors [1–7]. When the electronic states are localized as in the Mott state, a charge-ordered-type modulation appears due to intersite Coulomb interactions. Moreover, a charge modulation can be induced by the Peierls instability—the so-called charge-density wave (CDW). In a system with heavy elements such as $5d$ transition metals, the large spin-orbit interaction can stabilize the localized spin-orbit Mott state, as observed in the $5d$ transition-metal compounds, and then the charge-ordered Mott state leads to a novel framework of the interplay [3,8].

A CDW-like structural transition was reported in the $5d$ transition-metal chalcogenide IrTe₂ at $T_s \sim 280$ K [9,10]. This has attracted a great deal of interest because of the recent discovery of superconductivity in Pt- and Pd-substituted or intercalated compounds [11–16]. With increasing Pt substitution, the structural transition is suppressed and a superconducting dome appears in the region of $0.04 \leqq x \leqq 0.12$, indicating similar diagrams to those of other unconventional supercon-

ductors. Although numerous studies have followed these initial works, a consensus about the mechanism for this structural transition is still lacking. The phase transition of IrTe₂ ($x = 0.0$) is accompanied by the emergence of a superstructure lattice modulation [12], with wave vector $\mathbf{Q}_{1/5} = (1/5\ 0\ -1/5)$ as expressed in reciprocal-lattice units in trigonal notation, which is illustrated in Fig. 1. The main elements are the Ir-Ir dimerization along the a axis with period $5a$, and the consequent distortion of the triangular Ir sublattice in the a-b plane, occurring together with a trigonal-to-triclinic symmetry reduction. The Ir-Ir dimerization stabilizes a unique stripelike order, with stripes running along the b axis, as indicated by x-ray diffraction [17–20], extended x-ray absorption fine structure [21], and resonant x-ray scattering [22] studies. Since in IrTe₂ the formal valence of Ir is $+4$, the Ir $5d$ electrons with a t_{2g} configuration are the closest to the chemical potential, and they are thus expected to play a central role in the CDW. However, photoemission and optical studies have shown that the charge-transfer energy in IrTe₂ is close to zero, and that the Te $5p$ states are also important for the low-energy physics [23–25]. In addition, recent x-ray diffraction (XRD) [8,19] and scanning tunneling microscopy (STM) [27] experiments revealed a further stepwise charge-ordering transition from $\mathbf{Q}_{1/5}$ to $\mathbf{Q}_{1/8} = (1/8\ 0\ -1/8)$ and/or $\mathbf{Q}_{1/11} = (1/11\ 0\ -1/11)$ below $T \sim 200$ K, while many studies reported that the $\mathbf{Q}_{1/5}$-type superstructures survived at their lowest temperatures [17,20,22]. Results from these studies also suggested that a
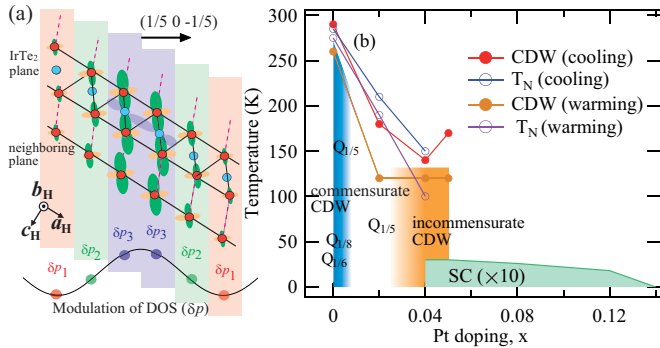
*ktakubo@issp.u-tokyo.ac.jp

FIG. 1. (a) Superstructure modulation of IrTe$_2$ with wave vector $\mathbf{Q}_{1/5} = (1/5\ 0\ -1/5)$, as expressed in reciprocal-lattice units in tetragonal notation [22]. The modulation of the density of states (DOS), highlighting an Ir-Ir dimerization, is shown at the bottom. (b) Phase diagram of Ir$_{1-x}$Pt$_x$Te$_2$. Points denoted as CDW were obtained in this study. T_N and the superconducting region are from Ref. [14].

CDW occurs at both of the Ir and Te sites, at least near its surface region. Furthermore, in some studies, differences of the electronic state between surface and bulk states for IrTe$_2$ have been reported. In another recent STM study for nonsubstituted IrTe$_2$, a superconducting domain coexisting with very complex charge-ordering structures that only exist in the surface region was reported [28]. An exotic one-dimensional surface state was also observed in angular-resolved photoemission spectra by Ootsuki *et al.* [29].

Moreover, a complex picture can be assumed for the relationship between such elusive CDW orders and superconducting orders in Pt-substituted Ir$_{1-x}$Pt$_x$Te$_2$. Because the phase diagram of Ir$_{1-x}$Pt$_x$Te$_2$ exhibits a diagram similar to those of other unconventional superconductors, the idea of a quantum critical point inside the superconducting dome can be considered [11]. However, it has been observed that many other transition-metal chalcogenides exhibit the coexistence of superconductivity with incommensurate CDW orders, where disorder effects and incommensuration of the CDWs were suggested to be more important [30–35]. In the intercalated 1T-TaS$_2$ and 1T-TiSe$_2$ systems, the superconductivity only coexists with incommensurate CDWs, although their mother compounds exhibit commensurate CDWs [31,32,35].

To revisit the superstructures in Ir$_{1-x}$Pt$_x$Te$_2$ and to clarify the relation between superconductivity and superstructural modulation in the bulk region, we studied the spatial ordering of electronic states by means of bulk-sensitive methods: resonant elastic and inelastic x-ray scattering at the edges of both Ir and Te. As a result, superstructure peaks with wave vectors of $\mathbf{Q} = (1/5\ 0\ -1/5)$, $(1/8\ 0\ -1/8)$, and $(1/6\ 0\ -1/6)$ are found on IrTe$_2$ ($x = 0.0$) at the lowest temperature, which are governed by the cooling speeds. In contrast, the incommensurate ordering peaks around $\mathbf{Q} = (1/5\ 0\ -1/5)$ are observed for doped samples of $0.02 < x \leqq 0.05$ at low temperature, suggesting that CDWs can coexist with superconductivity for $x = 0.05$. The resonant elastic and inelastic x-ray scattering results at the Ir and Te edges emphasize the importance of the Te 5p states rather than the Ir 5d states in the stripelike ordering formation in these systems.

II. EXPERIMENT

Single-crystal samples of Ir$_{1-x}$Pt$_x$Te$_2$ ($0 \leqq x \leqq 0.12$) were prepared using a self-flux method [14,16,25]. The cleaved (001) planes were used for all the scattering experiments. Resonant elastic x-ray scattering (REXS) at the Ir L_3 ($2p \rightarrow 5d$) absorption edge in the hard-x-ray region was performed at the Photon Factory's BL-4C. REXS at the Te L_1 ($2s \rightarrow 5p$) absorption edge was conducted at the BL-22XU of SPring-8. The polarization of incident x rays was perpendicular to the scattering plane. The samples were mounted so that [100] and [001] directions were in the scattering plane, although it was confirmed that the REXS spectra barely show the azimuthal dependence. Here, the reciprocal space indices ($h\ k\ l$) refer to the high-temperature trigonal unit cell. The x-ray absorption spectra (XAS) at the Ir L_3 and Te L_1 edges were recorded by their fluorescence.

On the other hand, resonant inelastic x-ray scattering (RIXS) at the Ir L_3 edges was carried out at the BL-11XU of SPring-8 [36]. Incident x rays were monochromatized by a double-crystal Si(111) monochromator and a secondary Si(844) channel-cut monochromator. Horizontally scattered x rays were analyzed in energy by a spherically diced and bent Si(844) crystal. The total energy resolution was about 70 meV. The spectra for horizontally polarized incident x rays were recorded near $2\theta \sim 86°$ so that elastic scattering was reduced [see Fig. 5(d)]. The sample was also mounted so that the [100] and [001] directions span the scattering plane.

REXS at the Te $M_{4,5}$ ($3d \rightarrow 5p$) edge in the soft-x-ray region was performed at the REIXS beamline of Canadian Light Source [37]. Single crystals were cleaved in vacuum to minimize surface contamination effects. The cleaved (001) plane was oriented at $\sim54°$ from the scattering plane in order to perform REXS measurements in the $Q = (h\ 0\ -h)$ plane. The polarization of the incident x ray was perpendicular to the scattering plane. XAS at the Te $M_{4,5}$ edges was recorded in the total electron yield (TEY) modes. The XAS results using the TEY mode showed no noticeable difference with respect to spectra acquired in total fluorescence yield mode.

III. RESULTS AND DISCUSSION

A. Superstructures in IrTe$_2$ ($x = 0.0$)

Figure 2 shows XRD along (0 0 −4) to (1 0 −5) through the superstructure peaks for IrTe$_2$ ($x = 0.0$) taken with $h\nu = 11.15$ keV, which is below the energy of the Ir L_3 absorption. The periods of the superstructures at low temperature depend strongly on the cooling protocols. As for the results of $x = 0.0$ shown in Fig. 2, the sample temperatures were continuously ramped down from $T = 300$ to 220 K with various tuned cooling rates and once XRD was measured at $T = 220$ K. Then the samples were cooling down again to $T = 10$ K at the same speeds. These measurements were conducted for a fresh sample each time, grown in a single batch. The measurements at $T = 10$ and 220 K took 1–2 h, including the time for alignment of the sample axes. When the cooling rate was set to 2 K/min, CDW-like superstructures with $\mathbf{Q}_{1/8} = (1/8\ 0\ -1/8)$ emerged at low temperature ($T = 10$ K), as shown in Fig. 2(b). While only the Bragg peaks were observable at $T = 300$ K [Figs. 2(b)–2(d)], the $\mathbf{Q}_{1/5} = (1/5\ 0\ -1/5)$-type ordering
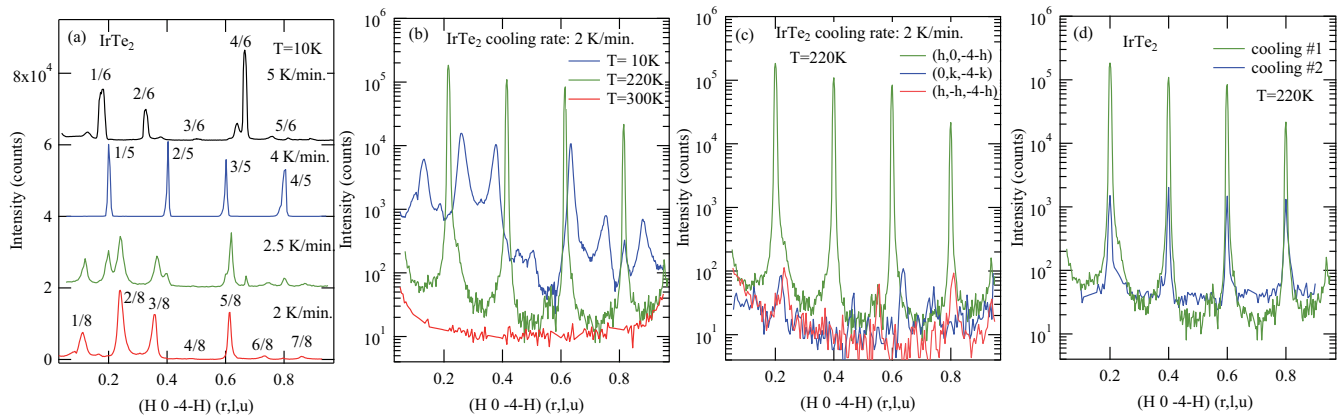
FIG. 2. $(H\ 0\ L)$ scan through the superstructure peaks for IrTe$_2$ ($x = 0.0$) taken with $h\nu = 11.15$ keV. (a) Superstructure peaks at $T = 10$ K obtained with various cooling rates: 2, 2.5, 4, and 5 K/min. (b) Temperature dependence of the superstructure peaks. The cooling rate was set to 2 K/min. (c) $(H\ 0\ L)$ scan along the three different crystal axes of $(h\ 0\ -4 - h)$, $(0\ k\ -4 - k)$, and $(h\ -h\ -4 - h)$ at $T = 220$ K. (d) Superstructure peaks at $T = 220$ K in the first and second cooling-warming cycles for the same sample. The cooling rates were 2 K/min.

peaks appeared at $T = 220$ K (below $T_s \sim 280$ K). Then, the modulation was subsequently changed to $\mathbf{Q}_{1/8}$-type below $T \sim 200$ K, although the $\mathbf{Q}_{1/5}$-type superstructures were reported for IrTe$_2$ in the previous studies for these samples at the lowest temperature [14,20,22]. Although some diffuse scatterings were observed along the $(H\ 0\ -H)$ reciprocal axis, the $\mathbf{Q}_{1/8}$-type ordering stabilized at $T = 10$ K. This observation is similar to the stepwise charge-ordering cascade reported by Ko *et al.* for samples synthesized by other groups [8]. Upon heating, the $\mathbf{Q}_{1/8}$ peaks remain up to $T \sim 290$ K and this phase directly transits to the high-temperature phase [8]. When the cooling speed was set to 4 K/min, however, the stepwise cascade transition to $\mathbf{Q}_{1/8}$ was not observed, and superstructures with $\mathbf{Q}_{1/5}$ were stabilized even at the lowest temperature of $T = 10$ K, as shown in Fig. 2(a), which is consistent with the previous reports for the same samples [20,22]. However, the coexistence of $\mathbf{Q}_{1/5}$ and $\mathbf{Q}_{1/8}$ could be obtained with a medium-cooling speed of 2.5 K/min. Finally, superstructures around $\mathbf{Q}_{1/6} = (1/6\ 0\ -1/6)$ coexisting with weak $\mathbf{Q}_{1/8}$ peaks appeared with the fastest cooling speed above 5 K/min. $\mathbf{Q}_{1/6}$ ordering for IrTe$_2$ has not been reported previously, while similar superstructures were obtained for IrTe$_{2-x}$Se$_x$ ($x > 0.3$) [19,26]. These observations strongly support a scenario of anionic depolymerization transition, as suggested by Oh *et al.* [26], where depolymerization-polymerization occur between the anionic Te-Te bonds across the transition. The covalence of the Te-Te bonds is partially lost across the transition, depolymerizing the Te-Te networks and leading to the diversity of superstructures.

The superstructures appear along one direction $(h\ 0\ -4 - h)$ of the triangular lattices and are not observable along the other two directions of $(0\ k\ -4 - k)$ and $(h\ -h\ -4 - h)$ as plotted in Fig. 2(c), indicating the formation of a single-domain structure with an x-ray spot size of ~ 1 mm^2. CDW distortion seemed to occur along one side of the triangular axis in these hard-x-ray experiments, although multidomain structures were reported in previous soft-x-ray and low-energy electron-diffraction experiments [22]. The evolution of the domain structures and superstructures seems to depend on the sample condition. Figure 2(d) shows the patterns at $T = 220$ K

of the first and second cooling-warming cycles taken for the same sample, which are normalized by the intensity of the Bragg peak of (004). The superstructure intensities at the second cooling attempt were 10^{-2} orders of magnitude smaller than those at the first attempt. Since the structural transition of IrTe$_2$ across T_s is very steep and can cause cracks in the crystal, long-range ordering would be weakened after the cooling cycle.

It should be noted that the pattern of the superstructures could also depend on many other subtle conditions. For example, the cracks mentioned above seem to change the thermal condition. We also tried the repeated—cooling and warming—measurements on a single sample but did not observe a clear reproducibility. However, $\mathbf{Q}_{1/8}$ superlattices were obtained in many cases, even when the cooling speeds were set to above 4 K/min. The thermal conductance from the cryostat would become worse by the cracks, and this tendency would still be consistent with the scenario of the cooling-rate dependence. In addition, the drift of the observations with time also appeared if the temperature was fixed at the range between $T = 80$ and 200 K. The diffuse scattering along the $(H\ 0\ -H)$ axis was sometimes observed at this temperature range (not shown). However, these drifts seemed to be very slow, taking several hours, and a clear reproducibility has not been obtained. A further study will be needed in order to clarify this point.

B. Doping dependence of the superstructure

Next, to clarify the relation between the CDW-like structural modulation and superconductivity, the evolution of the superstructure peaks with Pt doping is examined by XRD for Ir$_{1-x}$Pt$_x$Te$_2$. As for the results shown in Fig. 3, the averaged cooling rates were set to ~ 2.5 K/min. The measurements took ~ 10 min at each temperature. The modulation periods depend only slightly on the cooling speeds, and a cascade transition to $\mathbf{Q}_{1/8}$ was not observed for the doped samples ($0.02 \leqq x \leqq 0.05$). As can be seen, the CDW-like superstructures of $\mathbf{Q}_{1/5}$ are observed for $x = 0.02$ below $T \sim 140$ K. In addition, the superstructures around $\mathbf{Q}_{1/5}$ are also found in the $x = 0.04$ and 0.05 samples at low temperature. Although $x = 0.04$ shows
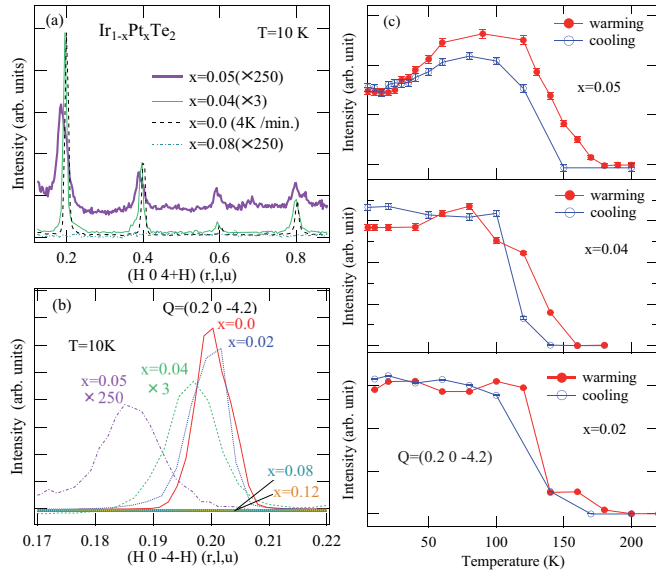
FIG. 3. (a) $(H\ 0\ L)$ scan through the superstructure peaks for $Ir_{1-x}Pt_xTe_2$ ($x = 0.0$, 0.04, and 0.05) taken with $h\nu = 11.15$ keV. (b) $(H\ 0\ L)$ scan through the superstructure peak of $\mathbf{Q} = (0.2\ 0 - 4.2)$ for $Ir_{1-x}Pt_xTe_2$ ($0.0 \leqq x \leqq 0.12$). (c) Temperature dependence around $\mathbf{Q} = (0.2\ 0 - 4.2)$ peaks for $x = 0.05$ (top), $x = 0.04$ (middle), and $x = 0.02$ (bottom), which were evaluated as the sum of the counts over the whole peak of $(0.2\ 0 - 4.2)$.

FIG. 4. REXS and XAS spectra at the Ir L_3 edges for (a) $IrTe_2$ ($x = 0.0$) and (b) $Ir_{0.96}Pt_{0.04}Te_2$ ($x = 0.04$). The calculated spectrum uses the lattice displacement model (see the main text).

some sample dependence of the structural and superconducting transition temperatures that may originate from its inhomogeneity [14,16], all the $x = 0.05$ samples including the batch used in this study show the superconductivity and do not show any anomaly at $T_s \sim 140$ K on the macroscopic conductivity and magnetization measurements [see Fig. 1(b)]. The superstructures for $x = 0.05$ are 10^{-2} orders of magnitude smaller than that for $x = 0.02$ but certainly observable around $\mathbf{Q}_{1/5}$. Four pieces of $x = 0.05$ crystals were investigated, and similar superlattices were found on all the pieces. The microscopic phase separation of the majority superconducting and minority charge-ordered domains may occur in the $x = 0.05$ samples. On the other hand, the superstructure disappears in $x = 0.08$ and 0.12 [Fig. 3(b)]. CDW with $\mathbf{Q}_{1/5}$ seems to persist to a higher doping level ($x \leqq 0.05$) than previously thought, and coexists with the superconducting state. Furthermore, CDW incommensuration is found along the $(H\ 0 - H)$ direction for $x = 0.04$ and 0.05 near the superconducting dome. Although the superstructures are perfectly commensurate with the lattice for $x = 0.0$ and 0.02, the peaks for $x = 0.04$ and 0.05 shift to the lower-H side. The peak widths also broaden as the doping level x increases. These observations are very similar to the results obtained for CDW in $1T$-TaS_2 [31] and $1T$-$TiSe_2$ [33,35] systems, where the incommensuration of CDWs also coincides with the onset of superconductivity. Both electron-phonon and electron-hole couplings have been suggested to play significant roles in these systems [35]. Therefore, similar mechanisms may also be important in driving the superconductivity of $Ir_{1-x}Pt_xTe_2$. Another possibility for driving the incommensurability of $x = 0.04$ and 0.05 is the coexistence of $\mathbf{Q}_{1/5}$- and $\mathbf{Q}_{1/8}$-type domains in the microscopic region, as observed in the STM studies for $IrTe_2$, where various
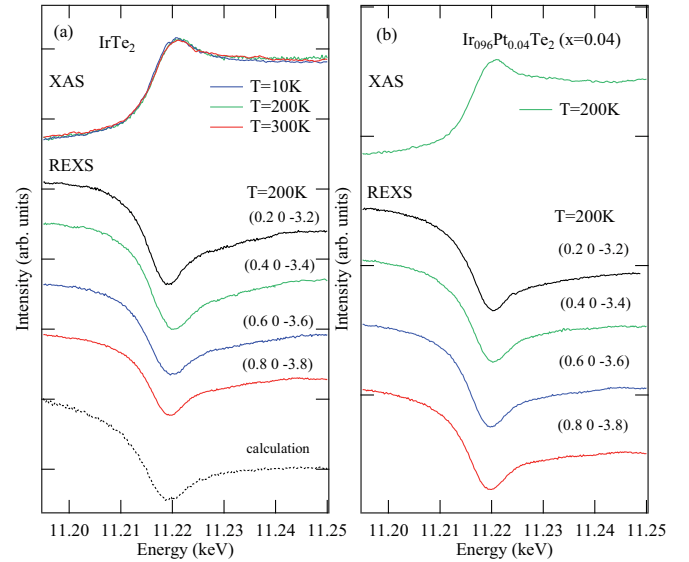
kinds of ordered domains coexist on nanometer scales [27,28]. Since the superconducting transition temperature at $x = 0.05$ is similar to those for $x > 0.05$ without CDWs, it is naturally speculated that the superconducting phase at $x = 0.05$ is different from the incommensurate CDW phase observed at $x = 0.04$ and 0.05. However, the incommensurability of CDWs shows that the phase separated $x = 0.05$ state is not a mere mixture of the commensurate CDW phase at $x = 0.0$ and the superconducting phase for $x > 0.05$. In this sense, the incommensurability of CDWs is associated with the emergence of superconductivity.

Figure 3(c) shows the detailed temperature dependence of the superstructure intensities around $\mathbf{Q}_{1/5}$ for $x = 0.02$, 0.04, and 0.05, measured across T_s during both cooling and warming cycles. The cooling-warming rates were set to ~ 4 K/min. The signals show sharp onsets having some hysteretic behaviors at $T_s \sim 150$ K for $x = 0.02$, $T_s \sim 140$ K for $x = 0.04$, and $T_s \sim 140$ K for $x = 0.05$, indicating the first-order character of these transitions. Furthermore, the intensity of the superstructures in superconducting $x = 0.05$ is suppressed below $T < 50$ K again. A similar suppression of the CDW intensities near the superconducting dome was reported for CDWs in high-temperature superconducting cuprates [4], indicating that these systems may harbor similar exotic phases.

C. REXS at the Ir L_3 edge

The spatial modulation of the electronic states in the Ir sites was investigated using the resonance at the Ir L_3 absorption at $h\nu \sim 12.2$ keV [15,38]. Figure 4 shows the REXS and x-ray absorption spectra for (a) $x = 0.0$ and (b) $x = 0.04$. However, no noticeable $\mathbf{Q}$ dependence is observed for the REXS spectra at the Ir L_3 edge. Although the REXS signals at the Te edges are resonantly enhanced in the XAS-peak region, as shown in Ref. [22] and later sections, only the dip structures were observed on REXS at the Ir L_3 edge. While the REXS

spectra for the Te edges can be modeled by using (i) valence modulation or (ii) energy shift models in the previous study [5,22], such dip structures on REXS without a **Q** dependence can only be reproduced by the calculation with (iii) a lattice displacement model such as given at the bottom of Fig. 4(a). In this calculation, the form factors $f(\omega)$ for different Ir and Te sites are evaluated from XAS. The wave vector (**Q**) and photon-energy (ω) -dependent structure factor $S(\mathbf{Q},\omega)$ are subsequently constructed based on the spatial modulation of $f(\omega)$ at different atomic positions $\mathbf{r}_j$:

$$S(\mathbf{Q},\omega) = \sum_j f_j(\omega) e^{-i\mathbf{Q}\cdot\mathbf{r}_j}. \tag{1}$$

In the lattice displacement model, the major contribution to $S(\mathbf{Q},\omega)$ originates from $\mathbf{r}_j = \mathbf{r}_j^0 + \delta\mathbf{r}_j$, where small displacements are used for the Ir and Te lattice sites in the modulated structure. Here, $f_j(\omega)$ are site-independent, i.e., no electronic modulation is assumed in the Ir sites. If $f_j(\omega)$ are assumed to have a modulation as large as ~0.3 eV, the calculated line shape exhibits a large **Q** dependence and conflicts with the present experimental observation (with further details of the calculation given in the Appendix). Therefore, these REXS results indicate that the electronic states in the Ir sites scarcely have spatial modulation, apparently contradicting the previous x-ray photoemission results [8,23,24]. Since REXS at the Ir L_3 edge is a highly bulk-sensitive technique compared to photoemission, the discrepancy may arise from the electronic structural difference between the bulk and surface regions suggested in the recent STM experiment [28]. The charge ordering in the Ir sites may only exist in their surface region, but the charge ordering in the bulk of $Ir_{1-x}Pt_xTe_2$ seems to occur in the Te orbitals rather than the Ir orbitals.

D. RIXS at the Ir L_3 edge

To further examine the electronic structural evolution in the Ir sites at the specific **Q** positions, RIXS spectra have been acquired with incident energies of $h\nu_i = 11.214$ keV near the top of the Ir L_3 edge. The data are shown in Figs. 5(a) and 5(b) for IrTe$_2$ and in Fig. 5(c) for Ir$_{0.95}$Pt$_{0.05}$Te$_2$ ($x = 0.05$). Distinct elastic diffraction ($E_{loss} = 0$) is observed at the superstructural positions of **Q** = (1.4 0 6.6) and (1.6 0 6.4) at $T = 200$ K (below T_s) for IrTe$_2$. The asymmetric line shape of the elastic peak comes from residual strain in the diced analyzers crystal. Some diffusive diffraction along $(h\ 0\ -h)$ is also observable at **Q** = (1.7 0 6.3) at $T = 200$ K. Strong fluorescence is observed around 2–4 eV energy loss at all positions, which is associated with hybridization effects between the transition-metal d and chalcogen p states [39,40]. In contrast, the d-d excitations across the Ir t_{2g} bands observed between 0.5 and 1.5 eV are very weak compared to those obtained for Ir oxides [36]. These observations indicate that the holes near the Fermi level and its spatial modulation reside in the Te orbitals rather than in the Ir orbitals and are consistent with the REXS results at the L_3 edge described before. Although the spectral change across T_s is very small, the tendency is similar to that observed in RIXS for CuIr$_2$S$_4$ across T_{MIT} [see the averaged (sum) spectrum in Fig. 5(c) and in Fig. 4 of Ref. [41]]. The spectral weight near the Fermi level ($E_{loss} \sim 0.5$ eV) is transferred into the higher-energy region of ~1.5 eV below T_s, qualitatively in
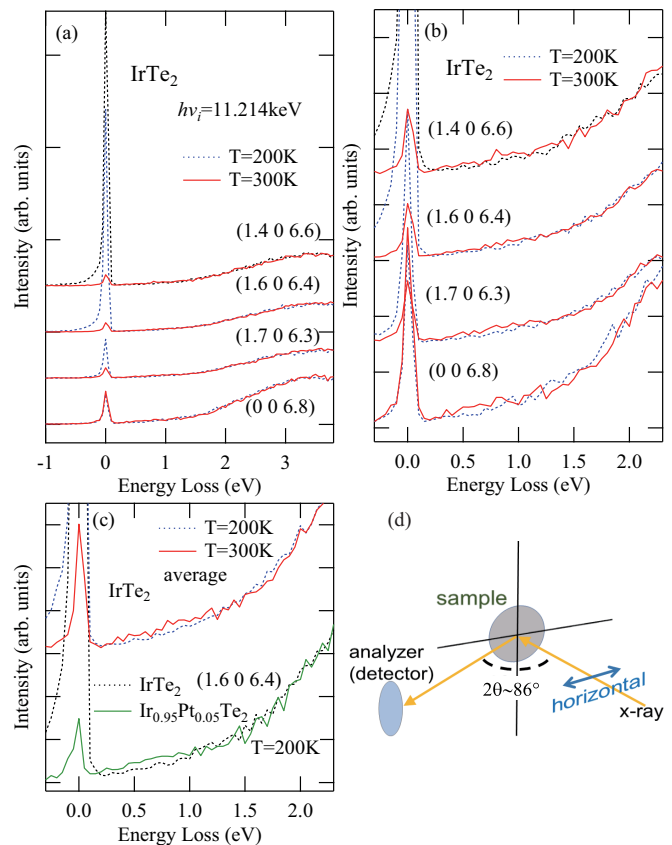

FIG. 5. RIXS of IrTe$_2$ and Ir$_{0.95}$Pt$_{0.05}$Te$_2$ with incident x-ray energies of $h\nu_i = 11.214$ keV at the Ir L_3 edges. (a) RIXS for IrTe$_2$ at the selected **Q** positions. (b) Enlarged view of RIXS in the low-energy-loss region. (c) Averaged spectra for IrTe$_2$ at $T = 200$ and 300 K, which are taken as an average of the spectra shown in (b) (upper). RIXS on **Q** = (1.6 0 6.4) for IrTe$_2$ and Ir$_{0.95}$Pt$_{0.05}$Te$_2$ at $T = 200$ K (lower). (d) Experimental geometry of RIXS.

agreement with the reconstruction of the band structure near the Fermi level up to 2 eV in the optical conductivity measurement [25]. In addition, the spectral difference between Ir$_{0.95}$Pt$_{0.05}$Te$_2$ ($x = 0.05$) and the low-temperature phase of IrTe$_2$ taken at $T = 200$ K is similar to the temperature dependence of IrTe$_2$ across T_s [Fig. 5(c)], indicating that these electronic evolutions definitely reflect the structural transition of these systems. The spectral shapes of the d-d excitation scarcely depend on the **Q** positions, which are also similar to the case of CuIr$_2$S$_4$ [41].

E. REXS at the Te M_5 and L_1 edges

Finally, the spatial modulation in the Te sites is investigated using REXS at the Te edges. Figure 6 shows (H 0 L) momentum scans and their temperature dependences through the resonant peak for Ir$_{1-x}$Pt$_x$Te$_2$ ($x = 0.0$, 0.04, and 0.05) at a photon energy of 571.3 eV, corresponding to the Te M_5 prepeak position. REXS signals on the superstructures around **Q** = (0.2 0 $-$0.2) are clearly observed on all samples of $x = 0.0$, 0.04, and 0.05 at low temperature, consistent with the hard-x-ray experiments described before. The CDW incommensurations, namely the peak shift to the lower-H side and the broadening of the widths, are also found on $x = 0.04$
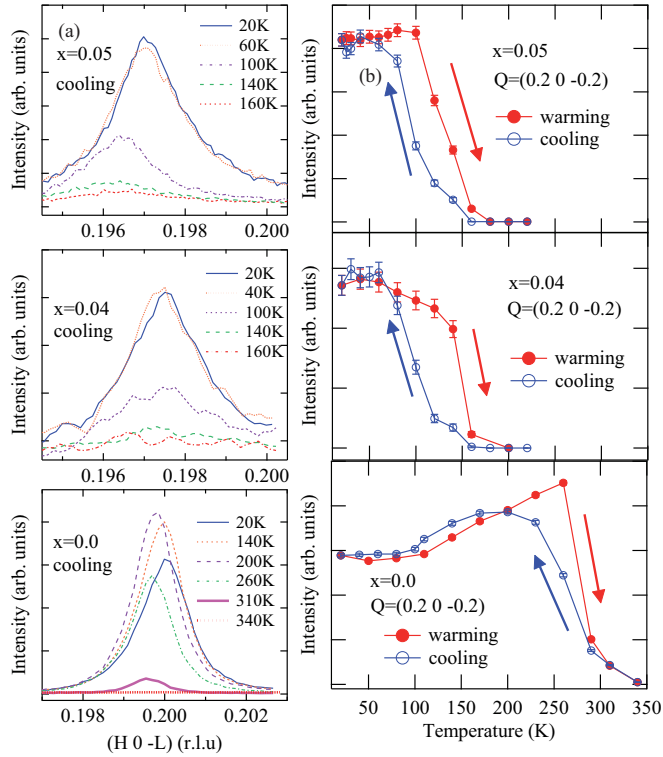
FIG. 6. Temperature dependence of REXS at the Te M_5 edges with 571.5 eV photons. (a) REXS ($H, 0, -L$) scan through the $\mathbf{Q} =$ (1/5 0 −1/5) superstructure peak measured on $Ir_{1-x}Pt_xTe_2$ [$x = 0.0$ (bottom), $x = 0.04$ (middle), and $x = 0.05$ (top)]. (b) Corresponding temperature dependence of the REXS intensity, which was evaluated as the sum of the counts over the whole peak of (0.2 0 − 0.2).

FIG. 7. Comparison between XAS and REXS spectra of the Te M–edge x-ray absorption for $Ir_{1-x}Pt_xTe_2$. (a) XAS spectra in the Te M_5 preedge region. Spectra for $x = 0.0$ (top), $x = 0.05$ (middle), and various compositions at $T = 300$ K (bottom). (b) REXS spectra in the Te M_5 preedge region for $x = 0.0$ and 0.05 at $T = 20$ K. (c) REXS spectra in the entire energy range of the Te M edge at 20 K.

and 0.05 near the onset of the superconducting dome. The cooling rates were ∼4 K/min, and the cascade transition to $\mathbf{Q}_{1/8}$ was not found in these soft-x-ray experiments. This difference could arise from the difference of the charge order between the surface and bulk region due to the different penetration depths for soft- and hard-x-ray experiments, while $\mathbf{Q}_{1/8}$-type order was reported on a surface-sensitive STM study by Hsu in Ref. [27]. Similar to the hard-x-ray experiment, all of the superstructural signals show sharp onsets at $T \sim 280$ K for $x = 0.0$, 130 K for $x = 0.04$, and 120 K for $x = 0.05$, respectively, indicating again the first-order character of these phase transitions.

Figure 7 shows the Te M_5 preedge spectra, which reflect the covalency between Te $5p$ and Ir $5d$ orbitals, or the unoccupied partial density of states (DOS) in the Te sites [22]. The XAS spectra at $T = 300$ K shift to higher energy as the doping x increases, indicating chemical potential shifts or electron dopings into the Te $5p$ orbitals induced by the Pt substitution [Fig. 7(a)]. The spectral change of XAS across the transition for IrTe₂ is consistent with the result of the band-structure calculations [18,20,23]. While the XAS spectra barely show any temperature dependence for $x = 0.05$, the energy-dependent line shape of REXS for $x = 0.05$ at $T = 20$ K is very similar to that for $x = 0.0$, as can be seen in Figs. 7(b) and 7(c). These features of REXS for $x = 0.0$, namely dip-hump structures at Te M, are evidence of the modulation of the unoccupied DOS for the five structurally inequivalent Te sites [22]. The charge
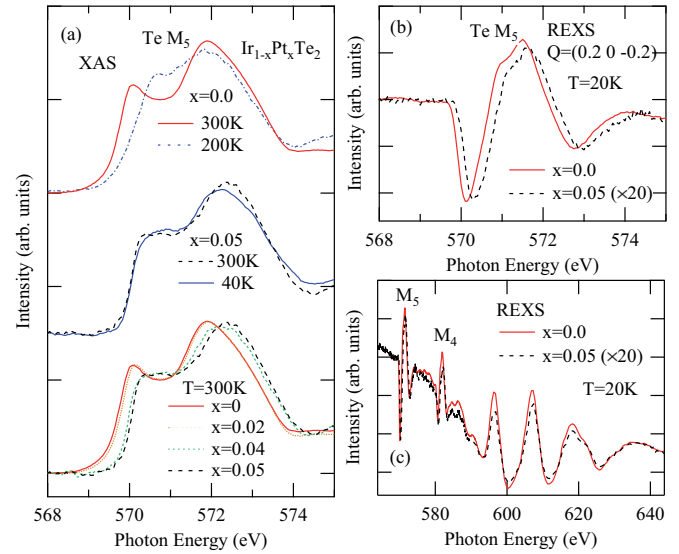
ordering in the Te sites of $x = 0.05$ will exist in the partial small domain, and the spatial modulation in it will be qualitatively similar to that for $x = 0.0$.

One may consider that REXS at the Te $M_{4,5}$ edges is a rather surface-sensitive technique comparable to the photoemission spectroscopy, since the Te $M_{4,5}$ edges are in the soft-x-ray
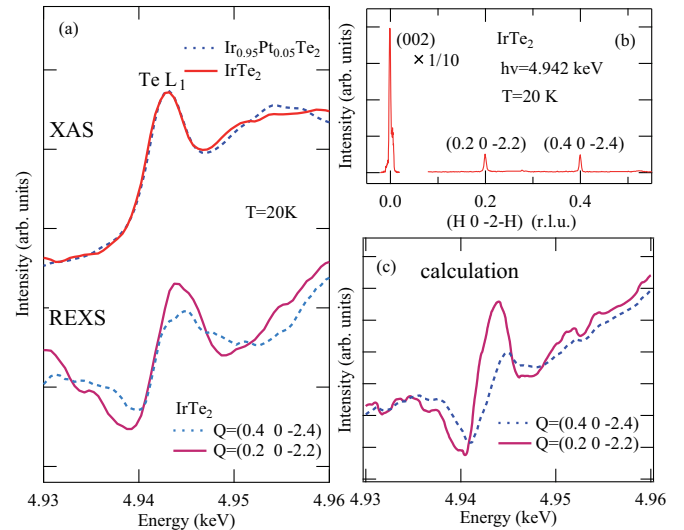

FIG. 8. (a) Comparison between XAS and REXS spectra of the Te L_1 absorption edge for $Ir_{1-x}Pt_xTe_2$. (b) Corresponding REXS ($H 0 L$) scan through the superstructure peaks at $T = 20$ K. (c) Calculated REXS intensity for the combination of a valence-modulation model (resonant term) with nonresonant lattice displacements for $\mathbf{Q} =$ (0.2 0 −2.2) and $\mathbf{Q} =$ (0.4 0 −2.4) (see the discussion in the main text).

region. Then the fact that the charge modulation on REXS is observed at Te $M_{4,5}$ but not at the Ir L_3 edge will not reflect the difference between the Te and Ir sites. However, the dip-hump structure and **Q**-dependent line shape are also observed in the bulk-sensitive REXS at the Te L_1 edge, as shown in Fig. 8. The XAS and REXS spectra at the Te L_1 edge for IrTe$_2$ are plotted in Fig. 8(a), and a corresponding momentum scan is plotted in Fig. 8(b). The signals of REXS on **Q** = (0.2 0 − 2.2) and (0.4 0 − 2.4) are resonantly enhanced at the Te L_1 edge, and the dip features are observed before the peak structures, which is just similar to REXS at the Te M_5 edge. In addition, REXS at the Te L_1 edge exhibits a certain **Q** dependence, in contrast to the case for the Ir L_3 edge. The resonant enhancement at the L_1 peak of **Q** = (0.4 0 − 2.4) is indistinctive compared to that of **Q** = (0.2 0 − 2.2), while the dip structures are noticeable at both positions. These line shapes for IrTe$_2$ can be modeled by the valence-modulation model with just the same parameters for REXS at the Te M edges given in Ref. [22] [Fig. 8(c)]. In the valence-modulation model, the major contribution to $S(\mathbf{Q},\omega)$ arises from $f_j(\omega) = f(\omega, p + \delta p_j)$, where δp_j is the variation in the local valence of the Te ions. The parameters are $\delta p_2 = -0.6, \delta p_3 = -0.6, \delta p_5 = -0.15, \delta p_1 = 0.9$, and $\delta p_4 = -0.15$ and are proportional to the local DOS at the Te sites, which are illustrated in Fig. 1(a). Therefore, we safely conclude that the spatial charge modulation of IrTe$_2$ exists in the Te sites even in the bulk region, following the striped formation with $\mathbf{Q}_{1/5} = (1/5\ 0\ -1.5)$.

IV. SUMMARY

We have examined the charge modulation of the Ir and Te sites in Ir$_{1-x}$Pt$_x$Te$_2$ by means of the resonant x-ray-scattering technique. The **Q** = (1/5 0 −1/5)-, (1/8 0 −1/8)-, and (1/6 0 −1/6)-type superstructures are observed for IrTe$_2$ ($x = 0.0$) at low temperature. The superstructures around $\mathbf{Q}_{1/5} = (1/5\ 0\ -1/5)$ coexist with the superconducting phase for Ir$_{1-x}$Pt$_x$Te$_2$ ($x = 0.05$), suggesting CDWs persist to higher Pt substitution than previously thought. The incommensuration of CDWs is observed for $x = 0.04$ and 0.05 samples, which coincide with the onset of the superconductivity. The REXS and RIXS spectra for the Ir L_3 edge scarcely depend on the wave vectors, while REXS spectra at the Te edges indicate the spatial charge modulation on the Te sites. The charge modulation in the bulk regions seems to reside in the Te orbitals rather than the Ir orbitals.

ACKNOWLEDGMENTS

APPENDIX: DETAIL OF THE CALCULATION OF REXS INTENSITY

The calculation of the REXS intensity is structured similarly to the method in the previous REXS study for IrTe$_2$ at the Te M edges [22]. The details were presented in the supplementary material of Ref. [22], thus the essential parts are pointed out here. The scattering intensity can be expressed as

$$I_{\text{REXS}} = \frac{C|S(\mathbf{Q},\omega)|^2}{\mu(\omega)}. \tag{A1}$$

The calculation is performed for three different methods [5], namely (i) *the valence modulation model*, corresponding to a periodic variation in the local valence of Ir or Te ions; (ii) *the energy shift model*, assuming a spatial modulation in the energy of the Ir $5d$ or Te $5p$ states; and (iii) *the lattice displacement model*, where small displacements are used for the Te and Ir lattice sites in the supermodulated structure. These models are subsequently implemented in the calculation of the structure factor $S(\mathbf{Q},\omega)$, which is written generally as Eq. (1) in the main text. In Eq. (1), r_j^0 is the position vector in the undistorted structure at site j, and δr_j is the displacement from the lattice position due to the structural modulation. The atomic form factor can also depend on additional parameters related to the electronic structure of the atom at j, such as the local charge density or energy levels; these factors are explicitly included in the respective models. More specifically, all the energy-dependent terms are included in the atomic form factor $f_j(\omega)$, while the atomic positions or displacements are of course energy-independent.

The form factor Im$\{f_j(\hbar\omega)\}$ can be determined from the XAS spectra, which are offset and scaled to calculated values of the absorption coefficient $\mu(\omega)$ (from NIST [42]) in order to express $\mu(\omega)$ in units of μm^{-1}. Via the optical theorem, Im$\{f_j(\omega)\}$ is linearly proportional to the absorption coefficient $\mu(\omega)$, and Re$\{f_j(\omega)\}$ can be determined from Im$\{f_j(\omega)\}$ using Kramers-Kronig transformations. Accordingly, to express $f(\omega)$ in electrons/atom, experimental XAS have been scaled and extrapolated to high and low energy using tabulated calculations of Im$\{f_j(\omega)\}$ above and below the absorption edge.
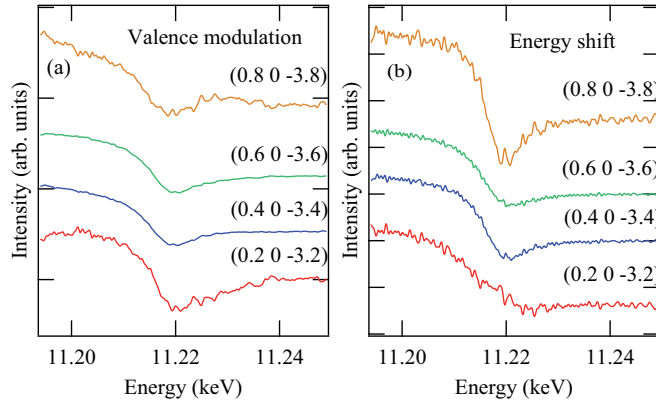
FIG. 9. Calculated REXS intensity using the (a) valence modulation and (b) energy shift models at the Ir L_3 edge.

1. Valence modulation model

The valence (or local DOS) modulation model takes into account spatial modulations in the local DOS at the Ir and Te sites as

$$S = \sum_{j=1}^{5} \left[\exp\left(\frac{-2j\pi i}{5} \right) f(\omega, p + \delta p_j) \right]. \quad (A2)$$

We determine $f(\omega, p_j)$ as a function of the local DOS modulation p_j by performing a linear extrapolation from the $f(\omega)$ measured with XAS at 300 K (HT phase) and 200 K (LT phase). The scattering intensity is given by

$$I = \frac{C}{\mu(\omega)} \left| \sum_{j=1}^{5} \left[\exp\left(\frac{-2j\pi i}{5} \right) f(\omega, p_j) \right] \right|^2. \quad (A3)$$

The corresponding calculation for the Ir L_3 edge, shown in Fig. 9(a), uses parameters $\delta p_1 = -0.6$, $\delta p_2 = -0.6$, $\delta p_3 = -0.15$, $\delta p_4 = 0.9$, and $\delta p_5 = -0.15$, which were used in the previous study. However, the results have a certain Q dependence and cannot reproduce the experimental feature for the Ir L_3 edge. On the other hand, these models with nonresonant lattice displacement terms describe well the REXS results at the Te M in the previous study [22] and L_1 edges as discussed in Sec. III E.

2. Energy shift model

Secondly, the energy shift model is considered. The difference with the valence modulation model is that here we use the spatial variation of the energy shift in place of the local DOS; in this case, the structure factor for the Ir-striped model is given by

$$S = \sum_{j=1}^{5} \left[\exp\left(\frac{-2j\pi i}{5} \right) f(\hbar\omega + \Delta E_j) \right]. \quad (A4)$$

Therefore the scattering intensity can be written as

$$I = \frac{C}{\mu(\omega)} \left| \sum_{j=1}^{5} \left[\exp\left(\frac{-2j\pi i}{5} \right) f(\hbar\omega + \Delta E_j) \right] \right|^2. \quad (A5)$$

The calculated results for Ir L_3 using this model are shown in Fig. 9(b) with $\Delta E_1 = -0.3$ eV, $\Delta E_2 = -0.05$ eV, $\Delta E_3 = 0.2$ eV, $\Delta E_4 = 0.2$ eV, and $\Delta E_5 = -0.05$ eV, the parameters of which were used in the previous study for the Te M_5 edge. However, the **Q** dependence appeared in this calculation similar to the valence modulation model, and therefore REXS at the Ir L_3 edge cannot be described within this model.

3. Lattice displacement model

For the lattice displacement model, f_j is the same at each site, but the lattice positions are displaced, i.e., $\boldsymbol{r}_j = \boldsymbol{r}_j^0 + \delta \boldsymbol{r}_j$. Considering a chain of 5 Te and/or Ir sites separated by $(a_H, 0, -c_H) \sim (0,0,c_L/5)$, the structure factor is given by

$$S = \sum_{j=1}^{5} \left[\exp\left(\frac{-2j\pi i}{5} + \frac{\delta_j}{c_L} \right) \right] f(\omega). \quad (A6)$$

In the limit of small displacements, we can expand the exponential terms to first order and write the REXS intensity as

$$I \cong \frac{4\pi^2 C}{\mu(\omega) c_L^2} \left| \sum_{j=1}^{5} \left[\exp\left(\frac{-2j\pi i}{5} \right) \delta_j \right] f(\omega) \right|^2 \quad (A7)$$

$$\propto \frac{|f(\omega)|^2}{\mu(\omega)}. \quad (A8)$$

This result holds even if one includes higher-order terms in the series expansion. Moreover, the magnitude of the displacements has no impact on the energy nor **Q** dependence of the calculated scattering intensity, since no modulation was assumed in the electronic state of each site or $f(\omega)$. The calculated result for the Ir L_3 edge using the lattice displacement model is plotted at the bottom of Fig. 4(a) and well reproduced the experimental result. On the other hand, the REXS at the Te L_1 edge cannot be reproduced by this model, since the experimental results exhibit a certain **Q** dependence, as discussed in the main text.

[1] J. M. Tranquada, B. J. Sternlieb, J. D. Axe, Y. Nakamura, and S. Uchida, Nature (London) **375**, 561 (1995).

[2] T. Mizokawa, L. H. Tjeng, G. A. Sawatzky, G. Ghiringhelli, O.

Tjernberg, N. B. Brookes, H. Fukazawa, S. Nakatsuji, and Y. Maeno, Phys. Rev. Lett. **87**, 077202 (2001).

[3] B. J. Kim, H. Jin, S. J. Moon, J.-Y. Kim, B.-G. Park, C. S.

Leem, J. Yu, T. W. Noh, C. Kim, S.-J. Oh, J.-H. Park, V. Durairaj, G. Cao, and E. Rotenberg, Phys. Rev. Lett. **101**, 076402 (2008).

[4] G. Ghiringhelli, M. Le Tacon, M. Minola, S. Blanco-Canosa, C. Mazzoli, N. B. Brookes, G. M. De Luca, A. Frano, D. G. Hawthorn, F. He, T. Loew, M. Moretti Sala, D. C. Peets, M. Salluzzo, E. Schierle, R. Sutarto, G. A. Sawatzky, E. Weschke, B. Keimer, and L. Braicovich, Science **337**, 821 (2012).

[5] A. J. Achkar, F. He, R. Sutarto, J. Geck, H. Zhang, Y.-J. Kim, and D. G. Hawthorn, Phys. Rev. Lett. **110**, 017001 (2013).

[6] R. Comin, A. Frano, M. M. Yee, Y. Yoshida, H. Eisaki, E. Schierle, E. Weschke, R. Sutarto, F. He, A. Soumyanarayanan, Y. He, M. Le Tacon, I. S. Elfimov, J. E. Hoffman, G. A. Sawatzky, B. Keimer, and A. Damascelli, Science **343**, 382 (2014).

[7] R. Comin, R. Sutarto, E. H. da Silva Neto, L. Chauviere, R. Liang, W. N. Hardy, D. A. Bonn, F. He, G. A. Sawatzky, and A. Damascelli, Nat. Mater. **14**, 796 (2015).

[8] K.-T. Ko, H.-H. Lee, D.-H. Kim, J.-J. Yang, S.-W. Cheong, M. J. Eom, J. S. Kim, R. Gammag, K.-S. Kim, H.-S. Kim, T.-H. Kim, H.-W. Yeom, T.-Y. Koo, H.-D. Kim, and J.-H. Park, Nat. Commun. **6**, 7342 (2015).

[9] S. Jobic, R. Brec, and J. Rouxel, J. Solid State Chem. **96**, 169 (1992).

[10] N. Matsumoto, K. Taniguchi, R. Endoh, H. Takano, and S. Nagata, J. Low. Temp. Phys. **117**, 1129 (1999).

[11] S. Pyon, K. Kudo, and M. Nohara, J. Phys. Soc. Jpn. **81**, 053701 (2012).

[12] J. J. Yang, Y. J. Choi, Y. S. Oh, A. Hogan, Y. Horibe, K. Kim, B. I. Min, and S.-W. Cheong, Phys. Rev. Lett. **108**, 116402 (2012).

[13] Y. P. Qi, S. Matsuishi, J. G. Guo, H. Mizoguchi, and H. Hosono, Phys. Rev. Lett. **109**, 217002 (2012).

[14] S. Pyon, K. Kudo, and M. Nohara, Physica C **494**, 80 (2013).

[15] M. Kamitani, M. S. Bahramy, R. Arita, S. Seki, T. Arima, Y. Tokura, and S. Ishiwata, Phys. Rev. B **87**, 180501 (2013).

[16] K. Kudo, M. Kobayashi, S. Pyon, and M. Nohara, J. Phys. Soc. Jpn. **82**, 085001 (2013).

[17] H. Cao, B. C. Chakoumakos, X. Chen, J. Yan, M. A. McGuire, H. Yang, R. Custelcean, H. Zhou, D. J. Singh, and D. Mandrus, Phys. Rev. B **88**, 115122 (2013).

[18] G. L. Pascut, K. Haule, M. J. Gutmann, S. A. Barnett, A. Bombardi, S. Artyukhin, T. Birol, D. Vanderbilt, J. J. Yang, S.-W. Cheong, and V. Kiryukhin, Phys. Rev. Lett. **112**, 086402 (2014).

[19] G. L. Pascut, T. Birol, M. J. Gutmann, J. J. Yang, S.-W. Cheong, K. Haule, and V. Kiryukhin, Phys. Rev. B **90**, 195122 (2014).

[20] T. Toriyama, M. Kobori, Y. Ohta, T. Konishi, S. Pyon, K. Kudo, M. Nohara, K. Sugimoto, T. Kim, and A. Fujiwara, J. Phys. Soc. Jpn. **83**, 033701 (2014).

[21] B. Joseph, M. Bendele, L. Simonelli, L. Maugeri, S. Pyon, K. Kudo, M. Nohara, T. Mizokawa, and N. L. Saini, Phys. Rev. B **88**, 224109 (2013).

[22] K. Takubo, R. Comin, D. Ootsuki, T. Mizokawa, H. Wadati, Y. Takahashi, G. Shibata, A. Fujimori, R. Sutarto, F. He, S. Pyon, K. Kudo, M. Nohara, G. Levy, I. S. Elfimov, G. A. Sawatzky, and A. Damascelli, Phys. Rev. B **90**, 081104(R) (2014).

[23] T. Qian, H. Miao, Z. J. Wang, X. Liu, X. Shi, Y. B. Huang, P. Zhang, N. Xu, P. Richard, M. Shi, M. H. Upton, J. P. Hill, G. Xu, X. Dai, Z. Fang, H. C. Lei, C. Petrovic, A. F. Fang, N. L. Wang, and H. Ding, New J. Phys. **16**, 123038 (2014).

[24] D. Ootsuki, Y. Wakisaka, S. Pyon, K. Kudo, M. Nohara, M. Arita, H. Anzai, H. Namatame, M. Taniguchi, N. L. Saini, and T. Mizokawa, Phys. Rev. B **86**, 014519 (2012).

[25] A. F. Fang, G. Xu, T. Dong, P. Zheng, and N. L. Wang, Sci. Rep. **3**, 1153 (2013).

[26] Y. S. Oh, J. J. Yang, Y. Horibe, and S.-W. Cheong, Phys. Rev. Lett. **110**, 127209 (2013).

[27] P.-J. Hsu, T. Mauerer, M. Vogt, J. J. Yang, Y. S. Oh, S-W. Cheong, M. Bode, and W. Wu, Phys. Rev. Lett. **111**, 266401 (2013).

[28] H. S. Kim, S. Kim, K. Kim, B. Il Min, Y.-H. Cho, L. Wang, S.-W. Cheong, and H. W. Yeom, Nano Lett. **16**, 4260 (2016).

[29] D. Ootsuki, S. Pyon, K. Kudo, M. Nohara, M. Horio, T. Yoshida, A. Fujimori, M. Arita, H. Anzai, H. Namatame, M. Taniguchi, N. L. Saini, and T. Mizokawa, J. Phys. Soc. Jpn. **82**, 093704 (2013).

[30] E. Morosan, H. W. Zandbergen, B. S. Dennis, J. W. G. Bos, Y. Onose, T. Klimczuk, A. P. Ramirez, N. P. Ong, and R. J. Cava, Nat. Phys. **2**, 544 (2006).

[31] B. Sipos, A. F. Kusmartseva, A. Akrap, H. Berger, L. Forró, and E. Tutiš, Nat. Mater. **7**, 960 (2008).

[32] Y. Liu, R. Ang, W. J. Lu, W. H. Song, L. J. Li, and Y. P. Sun, Appl. Phys. Lett. **102**, 192602 (2013).

[33] Y. I. Joe, X. Chen, P. Ghaemi, K. Finkelstein, G. de La Peña, Y. Gan, J. Lee, S. Yuan, J. Geck, G. MacDougall, T. C. Chiang, S. L. Cooper, E. Fradkin, and P. Abbamonte, Nat. Phys. **10**, 421 (2014).

[34] L. Li, E. O'Farrell, K. Loh, G. Eda, B. Özyilmaz, and A. C. Neto, Nature (London) **529**, 185 (2015).

[35] A. Kogar, G. A. de la Pena, S. Lee, Y. Fang, S. X.-L. Sun, D. B. Lioi, G. Karapetrov, K. D. Finkelstein, J. P. C. Ruff, P. Abbamonte, and S. Rosenkranz, Phys. Rev. Lett. **118**, 027002 (2017).

[36] K. Ishii, T. Tohyama, and J. Mizuki, J. Phys. Soc. Jpn. **82**, 021015 (2013), and references therein.

[37] D. G. Hawthorn, F. He, L. Venema, H. Davis, A. J. Achkar, J. Zhang, R. Sutarto, H. Wadati, A. Radi, T. Wilson, G. Wright, K. M. Shen, J. Geck, H. Zhang, V. Novk, and G. A. Sawatzky, Rev. Sci. Instrum. **82**, 073104 (2011).

[38] J. P. Clancy, N. Chen, C. Y. Kim, W. F. Chen, K. W. Plumb, B. C. Jeon, T. W. Noh, and Y.-J. Kim, Phys. Rev. B **86**, 195131 (2012).

[39] C. Monney, A. Uldry, K. J. Zhou, A. Krzton-Maziopa, E. Pomjakushina, V. N. Strocov, B. Delley, and T. Schmitt, Phys. Rev. B **88**, 165103 (2013).

[40] K. Takubo, Y. Yokoyama, H. Wadati, S. Iwasaki, T. Mizokawa, T. Boyko, R. Sutarto, F. He, K. Hashizume, S. Imaizumi, T. Aoyama, Y. Imai, and K. Ohgushi, Phys. Rev. B **96**, 115157 (2017).

[41] H. Gretarsson, J. Kim, D. Casa, T. Gog, K. R. Choi, S. W. Cheong, and Y.-J. Kim, Phys. Rev. B **84**, 125135 (2011).

[42] C. Chantler, J. Phys. Chem. Ref. Data **24**, 71 (1995).